Original Article

Artificial intelligence algorithm was used to establish and verify the prediction model of portal hypertension in hepatocellular carcinoma based on clinical parameters and imaging features

Yongfei He[1,2#], Qiang Gao[2,3#], Shutian Mo[2,4], Ketuan Huang[2], Yuan Liao[2], Tianyi Liang[2], Meifeng Chen[2], Jicai Wang[1], Qiang Tao[1], Guangquan Zhang[1], Fenfang Wu[1,5], Chuangye Han[2,4], Xianjie Shi[1], Tao Peng[2,4]

[1]Department of Hepatopancreatobiliary Surgery, The Eighth Affiliated Hospital of Sun Yat-sen University, Shenzhen, China; [2]Department of Hepatobiliary Surgery, the First Affiliated Hospital of Guangxi Medical University, Nanning, China; [3]Department of Hepatobiliary Surgery, Affiliated Hospital of Inner Mongolia Medical University, Hohhot, China; [4]Guangxi Key Laboratory of Enhanced Recovery After Surgery for Gastrointestinal Cancer, the First Affiliated Hospital of Guangxi Medical University, Nanning, China; [5]Biotherapeutic Clinical Research Center, Shenzhen Third People's Hospital, Shenzhen, China

Contributions: (I) Conception and design: T Peng; (II) Administrative support: C Han, X Shi; (III) Provision of study materials or patients: Y He, Q Gao; (IV) Collection and assembly of data: S Mo, K Huang, Y Liao, T Liang; (V) Data analysis and interpretation: M Chen, J Wang, Q Tao, G Zhang, F Wu; (VI) Manuscript writing: All authors; (VII) Final approval of manuscript: All authors.

[#]These authors contributed equally to this work.

Correspondence to: Tao Peng, PhD; Chuangye Han, PhD. Department of Hepatobiliary Surgery, the First Affiliated Hospital of Guangxi Medical University, Nanning, China; Guangxi Key Laboratory of Enhanced Recovery After Surgery for Gastrointestinal Cancer, the First Affiliated Hospital of Guangxi Medical University, No. 6 Shuangyong Road, Nanning 530021, China. Email: pengtaogmu@163.com; hanchuangye@hotmail.com; Xianjie Shi, PhD. Department of Hepatopancreatobiliary Surgery, The Eighth Affiliated Hospital of Sun Yat-sen University, 3025 Shennan Middle Road, Shenzhen 518033, China. Email: shixj7@mail.sysu.edu.cn.

Background: Portal hypertension (PHT) is an important factor leading to a poor prognosis in patients with hepatocellular carcinoma (HCC). Identifying patients with PHT for individualized treatment is of great clinical significance. The prediction model of HCC combined PHT is in urgent need of clinical practice. Combining clinical parameters and imaging features can improve prediction accuracy. The application of artificial intelligence algorithms can further tap the potential of data, optimize the prediction model, and provide strong support for early intervention and personalized treatment of PHT. This study aimed to establish a prediction model of PHT based on the clinicopathological features of PHT and computed tomography scanning features of the non-tumor liver area in the portal vein stage.

Methods: A total of 884 patients were enrolled in this study, and randomly divided into a training set of 707 patients (of whom 89 had PHT) and a validation set of 177 patients (of whom 23 had PHT) at a ratio of 8:2. Univariate and multivariate logistic regression analyses were performed to screen the clinical features. Radiomics and deep-learning features were extracted from the non-tumorous liver regions. Feature selection was conducted using *t*-tests, correlation analyses, and least absolute shrinkage and selection operator regression models. Finally, a predictive model for PHT in HCC patients was constructed by combining clinical features with the selected radiomics and deep-learning features.

Results: Portal vein diameter (PVD), Child-Pugh score, and fibrosis 4 (FIB-4) score were identified as independent risk factors for PHT. The predictive model that incorporated clinical features, radiomics features from non-tumorous liver regions, and deep-learning features had an area under the curve (AUC) of 0.966 [95% confidence interval (CI): 0.954–0.979] and a sensitivity of 0.966 in the training set, and an AUC of 0.698 (95% CI: 0.565–0.831) and a sensitivity of 0.609 in the validation set.

Conclusions: The preoperative evaluation showed that increased PVD, higher Child-Pugh score, and increased FIB-4 score were independent risk factors for PHT in patients with HCC. To predict the occurrence of PHT more effectively, we construct a comprehensive prediction model. The model incorporates clinical parameters, radiomic features, and deep learning features. This fusion of multi-modal

features enables the model to capture complex information related to PHT more comprehensively, thus achieving high prediction accuracy and practicability.

Keywords: Hepatocellular carcinoma (HCC); portal hypertension (PHT); radiomics; deep learning; prediction model

Submitted Nov 29, 2024. Accepted for publication Feb 11, 2025. Published online Feb 26, 2025.
doi: 10.21037/jgo-2024-931
View this article at: https://dx.doi.org/10.21037/jgo-2024-931

Introduction

Liver cancer is a global health challenge. It is estimated that 1 million individuals will be affected annually by liver cancer by 2025, with hepatocellular carcinoma (HCC) being the most common form, accounting for approximately 90% of cases (1,2). Surgical resection is the preferred treatment for primary HCC patients with good liver reserve function (3). However, portal hypertension (PHT) affects the choice of treatment for HCC, and clinically significant PHT is a predictor of post-hepatectomy liver failure and mortality (4). Research has shown that PHT may also be a predictor of postoperative HCC recurrence (5). Thus, the proper assessment and treatment of PHT is a key factor in improving the outcomes of HCC patients (6,7). There is an urgent need to accurately predict PHT to optimize preoperative treatment decisions for HCC patients.

Currently, the clinical surrogate standards for diagnosing PHT domestically and internationally mainly refer to imaging examinations, such as platelet (Plt) or white blood cell counts, spleen size, and esophageal and gastric varices, with a diagnosis of PHT made if two or more of these criteria are met (8). Domestic and international studies generally refer to the above diagnostic criteria, but a unified clinical standard for indirectly diagnosing PHT has not yet been specifically established (4).

Hepatic venous pressure gradient (HVPG) is currently the gold standard for accurately assessing changes in portal pressure internationally (9). However, HVPG is an invasive test with complex procedures and high costs, making it difficult to promote clinically. Moreover, HVPG only represents portal perfusion pressure, and actually reflects hepatic sinusoidal pressure not direct portal pressure (10). Direct puncture of the portal venous system, such as the right gastroepiploic vein, during surgery, can measure direct and reliable free portal pressure, but can only be used intraoperatively. Therefore, a non-invasive predictive tool that can identify PHT based on preoperative portal venous pressure (PVP) measurement would be highly beneficial and improve the perioperative management of HCC patients with PHT.

Clinicopathological factors used to assess predictors of PHT risk in HCC patients, including clinical parameters and imaging features, have improved understanding of PHT and contributed to clinical decision-making, but have limited predictors, insufficient accuracy, generality, and reproducibility. Therefore, we propose a high-accuracy prediction model combining clinical parameters, radiological characteristics, and deep learning techniques, aiming to provide new ideas and methods for the prediction

Highlight box

Key findings

- Preoperative assessment revealed that portal vein diameter (PVD), Child-Pugh score, and fibrosis 4 (FIB-4) score are independent risk factors for the development of portal hypertension (PHT) in hepatocellular carcinoma (HCC) patients. The model that included clinical, radiomics, and deep-learning features demonstrated high predictive accuracy and practicality.

What is known, and what is new?

- HCC patients with PHT are at a greater risk of undergoing surgery, but the prognosis for those undergoing surgery is comparable to that of those without PHT. Therefore, it is of great significance to accurately predict HCC patients with PHT before surgery.
- Based on the liver imaging and clinical features, we established a portal vein model for the preoperative prediction of HCC, which showed good predictive performance. In addition, the risk factors of PHT in HCC were also identified.

What is the implication, and what should change now?

- This study established a non-invasive predictive model for HCC with PHT to guide clinical treatment decisions, and to help screen suitable patients for surgical treatment to achieve a better prognosis.

and management of PHT in patients with HCC.

In recent years, the field of medical radiomics analysis has developed rapidly, resulting not only in an increase in the number of pattern recognition tools but also in an expansion in the scale of datasets. Various aspects of this field have been widely applied and deeply researched, including tumor detection, the automatic generation of structured diagnostic reports, the determination and quantitative assessment of disease properties, tumor feature extraction, and the precise localization of target organs in radiotherapy (11-14). Numerous studies have leveraged emerging radiomics technologies to significantly improve the accuracy of diagnosis, prognosis, and prediction in cancer research (15-18). Using artificial intelligence (AI) to determine the AIMMUNOx score, AImmunoscore (AIS)'s multi-stain deep learning model has strong prognostic ability, superior to other clinical, molecular, and immune cell-based parameters, and can also be used to predict the response of rectal cancer patients to neoadjuvant therapy, which is a valuable decision-making tool that can provide clinicians with tumor immune microenvironment-based (19). These studies have shown the immense potential of radiomics in early disease prediction and diagnosis.

With continuous advancements in AI, the use of deep learning has become increasingly prevalent in medical image analysis, and the fusion of medical imaging and AI is regarded as one of the fields with the greatest development potential (20,21). Deep transfer learning (DTL), as an efficient machine-learning strategy, can fully leverage previously accumulated knowledge and experience to address complex modeling challenges. A DTL method that combines deep learning with radiomics features has demonstrated significant results in predicting survival rates among patients with high-grade gliomas, particularly in distinguishing between long- and short-term survivors (22). Additionally, AI has shown excellent performance in the non-invasive prediction of PVP, providing an important auxiliary means for the diagnosis and treatment of PHT.

The prediction model of PHT plays an important role in improving the clinical outcome of HCC patients with PHT. By continuously optimizing and improving the predictive model, we can more accurately assess the disease and risk of patients and develop more reasonable treatment plans for patients, thereby improving the survival rate and quality of life of patients. Therefore, this study sought to explore the clinical features of PHT and the imaging features of portal phase liver computed tomography (CT) in non-tumor areas, establish and evaluate PHT prediction models using various methods, and comprehensively evaluate the advantages and shortcomings of different models in predicting efficacies, to provide strong support for clinical decision making. We present this article in accordance with the TRIPOD reporting checklist (available at https://jgo.amegroups.com/article/view/10.21037/jgo-2024-931/rc).

Methods

Study participants

The study was reviewed and approved by the Ethics Committee of the First Affiliated Hospital of Guangxi Medical University (No. 2023-E488-01). The study was conducted in accordance with the Declaration of Helsinki (as revised in 2013). Because the patient data were collected retrospectively, informed consent was not required. Retrospective data were collected from HCC patients who underwent open hepatectomy with intraoperative portal vein pressure measurements between January 2013 and January 2020 from the First Affiliated Hospital of Guangxi Medical University. To be eligible for inclusion in this study, the patients had to meet the following inclusion criteria: (I) be aged ≥18 and <70 years; and (II) have HCC confirmed by postoperative pathology. Patients were excluded from the study if they met any of the following exclusion criteria: (I) had no available preoperative contrast-enhanced liver CT scans; (II) had portal vein, splenic vein cancer thrombus, invasion of any large blood vessel, or arteriovenous fistula; (III) had postoperative recurrence, had liver cancer rupture and hemorrhage, or had previously undergone upper abdominal surgery or preoperative interventions [e.g., transcatheter arterial chemoembolization (TACE) and hepatic artery infusion chemotherapy (HAIC)], portal vein ligation, splenectomy, or splenic artery ligation; (IV) had missing preoperative important examination data; and/or (V) had other tumors. The normal range of portal pressure is usually between 13 and 24 cmH_2O. PHT was defined as a portal pressure level of 25 cmH_2O or more, and less than 25 cmH_2O is defined as non-PHT. The definition of PHT with a portal pressure of 25 cmH_2O is based on the normal range of portal pressure, the definition criteria of PHT, the clinical significance of PHT, and the relationship between PHT and cirrhosis. A total of 884 patients were included in the study and randomly assigned at a ratio of 8:2 to the training group (which comprised 707 patients, 89 of whom had PHT) and the validation group (which comprised

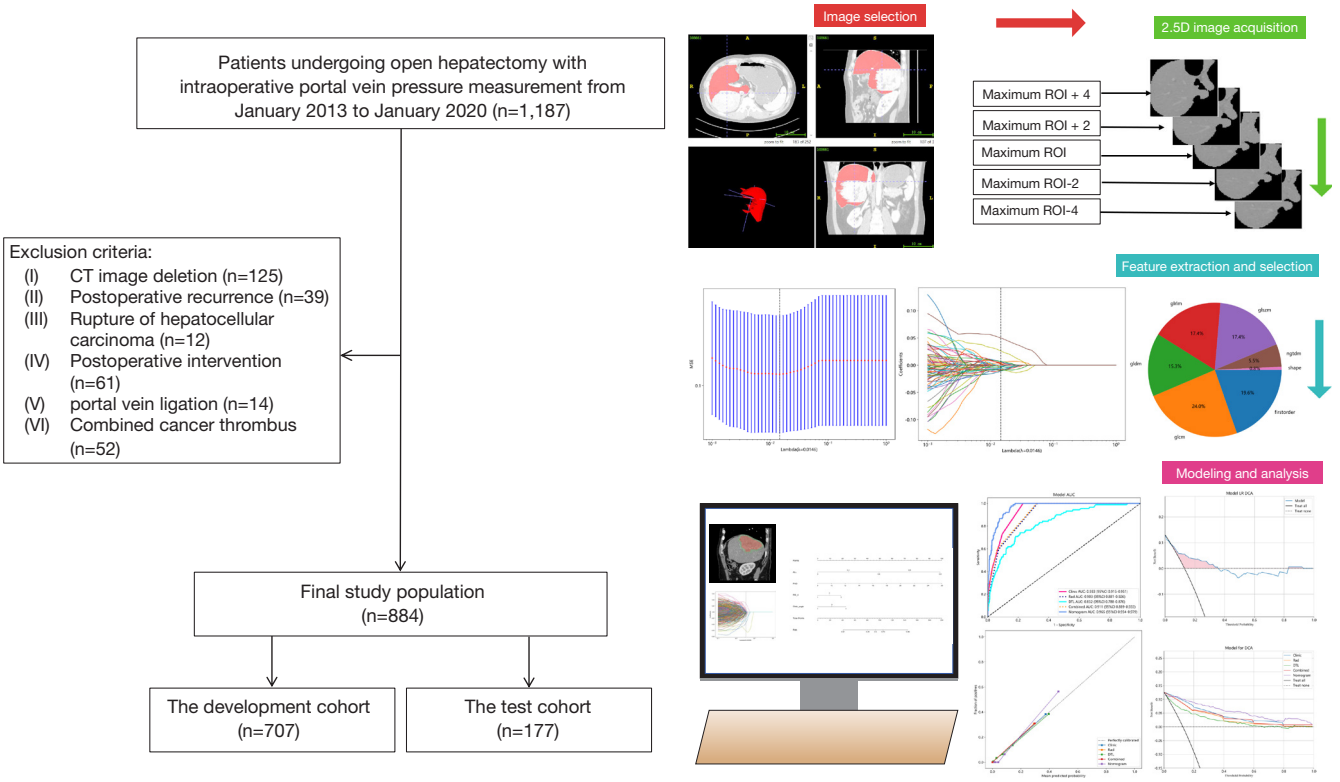

Figure 1 Flow chart showing the patient's tolerance criteria and the model's construction process. ROI, region of interest.

177 patients, 23 of whom had PHT) (*Figure 1*). The reasons for the small sample size are as follows: first, HCC and its complications, such as PHT, are relatively complex diseases, and their occurrence and development involve multiple factors. Therefore, it is not easy to collect patient data that meets the research criteria and has complete information. Secondly, this study has high requirements for data quality and needs to ensure the accuracy and consistency of data, which limits the expansion of sample size to a certain extent. Finally, due to time, resources, and ethical constraints, we cannot collect a large amount of patient data for verification in a short period.

Data collection and follow-up

The basic data, laboratory indicators, operation-related indicators, and CT image data of the patients were collected from the electronic medical record system, and the patients were followed-up through an outpatient system, imaging system, telephone calls, and other means to evaluate their postoperative recovery and recurrence according to criteria the Guidelines for Diagnosis and Treatment of Primary Liver Cancer (2019 edition) (3). The deadline for follow-up was December 31, 2023. Relapse-free survival was defined as the time from the date of surgery to recurrence or the last follow-up. Overall survival was defined as the time from the date of surgery to the patient's death or the last follow-up. For cases lacking important data, we deleted them. By identifying lost data, assessing the impact, selecting the appropriate processing method, verifying the processing effect, and reporting the processing process in detail, the impact of lost data on the analysis results can be minimized, and the accuracy and reliability of the data can be improved.

Enhanced CT scanning technology

The CT examination was performed using GE 64 LightSpeed VCT and Siemens dual-source CT scanners. Non-ionic contrast media (300 mg/mL) was used for enhanced scanning. A blob (3 mL/kg) of contrast agent was injected through a vein in the forearm at a rate of 2.5 mL/s using a high-pressure syringe. Arterial (22–30 s delay), venous (50–55 s delay), delayed (180 s delay), and continuous spiral scans (6–8 s delay) were acquired at 8 mm layer thickness,

120 kV tube voltage, 280 mA beam, and 0.5 revolutions per seconds. The images were stored in the Digital Imaging and Communications in Medicine format in the Picture Archiving and Communication System.

Radiomics feature extraction and selection

ITK – SNAP 4.0 software (http://www.itksnap.org/pmwiki/pmwiki.php) was used to select the region of interest (ROI) in the manual sketch, select the portal vein phase CT, and sketch the liver ROI. All ROI segmentation was carried out by two professional doctors. To evaluate the repeatability of the features, the same sketcher outlined the images of all patients, and segmentation was then repeated on the CT scans of 30 randomly selected patients, and the features were extracted. To evaluate the feature repeatability among the sketchers, another sketcher independently divided and extracted the features from the same 30 patients. Finally, the intraclass correlation coefficient (ICC) was calculated. Imaging features with high reproducibility (an ICC >0.8) were screened.

To reduce the interference and bias that tissues other than liver tissues might have on DTL, we erased the images of the surrounding tissues and mainly focused on the images of the liver. Using the maximum cross-section of the non-tumor area of the liver as a reference point, we selected images of the second and fourth layers toward the head, and similarly, the second and fourth layers toward the tail. Together, these five layers comprised a 2.5-day CT image of a patient's non-tumor area of the liver. This enabled us to focus more closely on the liver and reduce the confusion and interference that other tissues may cause when training the DTL model. Python language and the image omics processing library Pyradiomics (version 3.0.1; https://pyradiomics.readthedocs.io/en/2.1.2/) were used for the omics image preprocessing and image feature extraction (see Appendix 1).

Model development and testing

We established machine-learning prediction models. The features from the final selection were used to construct three machine-learning algorithm models; that is, a logistic regression (LR) model, K-nearest neighbor (KNN) model, and random forest model. Following an analysis of the performance of the three models, the KNN algorithm model was selected. In addition, to intuitively and effectively evaluate the incremental prediction value of deep-learning features and imaging omics features in terms of the clinical risk factors, we combined deep-learning features, imaging omics features, and clinical risk factors based on the LR regression analysis, and established a new linear prediction model based on pre-feature fusion, and then mapped a nomogram. Finally, we evaluated the performance of the model on the training and test sets. Receiver operating characteristic (ROC) curve, calibration, and clinical decision curves were used to evaluate the accuracy, calibration degree, and clinical applicability of the model, respectively.

The basic DTL algorithm design was created in Anaconda open-source software, based on the Python programming language Pytorch (https://pytorch.org/) open-source programming package. The selection of ResNet-50 as the backbone network for the DTL model and Adam as the optimizer is based on their combined advantages in terms of performance, generalization, and computational efficiency. These choices help to improve the overall performance and application of DTL models. The selected loss function was binary cross-entropy, the parameter optimizer was Adam, the learning rate was set to 0.0001, the AlphaDropout parameter was set to 0.5, the activation function was real, and the classification function was sigmoid. The Epoch for training was set to 50. After the Restnet50 was retrained, the model parameters were saved, and the test set was predictive classified.

Statistical analysis

The continuous variables were presented as the mean ± standard deviation, or the median spacing. Depending on whether the variables conformed to a normal distribution, the *t*-test or *U*-test was used to compare differences between the groups. The categorical variables were presented as the quantity (percentage), and differences between groups were compared using the Chi-squared test or Fisher's exact probability method. A principal component analysis, *t*-test, correlation analysis, and least absolute shrinkage and selection operator (LASSO) regression algorithm were used to reduce the dimensionality of the extracted image features, and the clinical features were screened by univariate analysis and multiple LR analysis to identify the most relevant clinical, imaging omics, and deep-learning features for predicting PHT. All statistical analyses were performed in R (version 4.2) and Python (version 3.9), and $P<0.05$ on both sides was considered statistically significant.

Results

Baseline data

We compared the preoperative clinical baseline data for PHT and non-PHT in the training and test sets, respectively. We found statistically significant differences between the PHT and non-PHT groups in the two datasets in terms of spleen volume, portal vein diameter (PVD), splenic vein diameter (SVD), Plt, hepatitis B virus NDA, Child-Pugh score and fibrosis 4 (FIB-4) (P<0.05). We also found statistically significant differences in the training set in terms of Plt, total bilirubin (Tbil), Child-Pugh score and FIB-4 (P<0.05) (*Table 1*).

Clinical feature screening

A univariate LR analysis of all preoperative clinical data was performed, and variables with P values <0.05 were included in the multivariate LR analysis. Variables with odds ratio (OR) values >1 and P values <0.05 were screened. Finally, PVD [OR: 1.027, 95% confidence interval (CI): 1.015–1.04, P<0.001], Child-Pugh (OR: 1.132, 95% CI: 1.05–1.221, P=0.01), and FIB-4 score (OR: 1.087, 95% CI: 1.048–1.126, P<0.001) were found to be independent risk factors for PHT (*Table 2*).

Radiomics features and deep-learning features

A total of 1,834 features were extracted, including 360 first order statistics (FOS) features and 440 grey level co-occurrence matrix (GLCM) features. Grey level run length matrix (GLRLM) 320 features, grey level size zone matrix (GLSZM) 320 features, neigbouring gray-tone difference matrix (NGTDM) features 100, gray level dependence matrix (GLDM) features 280, shape features 14 (Figure S1). After the *t*-test, correlation coefficient analysis, and LASSO regression, the corresponding image features of imagomics and deep learning were screened out. For the characteristic parameters of the model and their corresponding weighting coefficients (Tables S2,S3).

Performance evaluation of machine-learning algorithm models

Three machine-learning algorithm models (i.e., LR, KNN, and random forest) were constructed using the identified features, and their prediction efficiency was compared. The accuracy, area under the curve (AUC) value, sensitivity, specificity, positive predictive value, negative predictive value, accuracy rate, recall rate, and F1 score of each model were compared on the training set and test set. All three machine-learning models showed good performance. Due to the limitation of the data, we took the training group with a large amount of data as the standard, combined with the results of the machine learning algorithm model in the third part of this study, and finally selected the KNN algorithm with the best results. The KNN algorithm had the highest AUC value of 0.903 (95% CI: 0.881–0.926), 0.911 (95% CI: 0.889–0.933), 0.933 (95% CI: 0.915–0.951) in the PHT prediction of the LR, KNN, Random Forest with the training set (*Table 3*, *Figure 2*). When selecting the KNN model, it is necessary to consider the data characteristics, the importance of features, and the advantages of the model. KNN is popular because it is simple and intuitive, non-parametric, and flexible in local modeling. Evaluate performance through cross-validation and optimize parameters to handle missing values. Taken together, KNN becomes an effective option for handling complex data sets and preventing potential bias.

Pre-feature fusion linear model based on radiomics features, deep-learning features, and clinical features

In the machine-learning predictive model training set, the clinical features, radiomics features, and radiological joint deep-learning features were well-fitted. Similar results were found in the test set. A LR algorithm was used to combine the clinical features with the radiological deep-learning features to build a new linear prediction model (*Figure 3*). The performance of these different feature sets was compared under the KNN classifier, and the nomogram had the best results in the training set (AUC: 0.966). The correction curve showed a good calibration degree, and the prediction probability was highly consistent with the actual observation probability, which indicated that the prediction accuracy of the model was high. Our model also showed excellent performance in the analysis of clinical decision curves. Under different threshold settings, the model achieved higher net benefits (*Table 4*, *Figure 4*).

Discussion

In this study, we conducted univariate and multivariate regression analyses of preoperative clinical data, ultimately identifying PVD, Child-Pugh score, and FIB-4 score as independent risk factors for PHT. Additionally, we

Table 1 Clinical baseline data of PHT and non-PHT patients for development and test sets

Feature	Development cohort			Test cohort		
	Non-PHT	PHT	P value	Non-PHT	PHT	P value
Gender			0.19			0.73
Female	82 (13.27)	17 (19.10)		19 (12.34)	4 (17.39)	
Male	536 (86.73)	72 (80.90)		135 (87.66)	19 (82.61)	
Age (years)	49.76±11.20	50.43±10.17	0.45	48.76±11.30	52.26±11.04	0.18
BMI (kg/m^2)	22.51±3.08	22.90±3.64	0.6	22.94±3.32	23.89±3.66	0.27
Diabetes			0.62			0.84
No	588 (95.15)	83 (93.26)		149 (96.75)	23 (100.00)	
Yes	30 (4.85)	6 (6.74)		5 (3.25)	0	
NLR	2.26±1.33	2.47±1.14	0.005	2.65±3.12	2.38±0.82	0.59
Plt (10^9/L)	206.03±84.19	139.70±94.39	<0.001	200.84±80.32	120.28±71.98	<0.001
Tbil (mmol/L)	12.33±6.13	19.46±25.85	<0.001	12.68±6.71	16.19±8.22	0.031
Alb (g/L)	39.31±3.95	36.87±3.86	<0.001	39.37±4.24	39.95±5.19	0.95
Ascites			0.037			0.052
No	506 (81.88)	64 (71.91)		125 (81.17)	14 (60.87)	
Yes	112 (18.12)	25 (28.09)		29 (18.83)	9 (39.13)	
AST (U/L)	44.72±38.30	68.90±120.04	<0.001	49.76±40.30	42.13±27.81	0.28
ALT (U/L)	44.26±43.29	71.95±186.07	0.23	45.71±39.12	38.09±32.40	0.13
AST/ALT	1.25±1.82	1.35±0.77	0.003	1.27±0.88	1.21±0.49	0.66
APRI			<0.001			>0.99
≤2	575 (93.04)	70 (78.65)		142 (92.21)	21 (91.30)	
>2	43 (6.96)	19 (21.35)		12 (7.79)	2 (8.70)	
INR	0.99±0.11	1.04±0.11	<0.001	1.00±0.11	1.02±0.09	0.25
Child Pugh			<0.001			<0.001
A	576 (93.20)	61 (68.54)		136 (88.31)	13 (56.52)	
B	42 (6.80)	27 (30.34)		18 (11.69)	10 (43.48)	
C	0	1 (1.12)		0	0	
FIB-4 score			<0.001			<0.001
Grade 1: <1.45	411 (66.50)	31 (34.83)		104 (67.53)	6 (26.09)	
Grade 2: 1.45–3.25	172 (27.83)	28 (31.46)		39 (25.32)	11 (47.83)	
Grade 3: >3.25	35 (5.66)	30 (33.71)		11 (7.14)	6 (26.09)	
Viral hepatitis B			0.99			0.002
No	178 (28.80)	25 (28.09)		35 (22.73)	13 (56.52)	
Yes	440 (71.20)	64 (71.91)		119 (77.27)	10 (43.48)	
Viral hepatitis C			0.92			>0.99
No	609 (98.54)	87 (97.75)		150 (97.40)	22 (95.65)	
Yes	9 (1.46)	2 (2.25)		4 (2.60)	1 (4.35)	
Hepatitis B virus DNA (IU/mL)	559,224.67±2,130,042.60	1,033,299.27±2,602,084.38	0.053	403,645.64±857,289.22	246,966.86±282,990.96	0.53
AFP (ng/mL)			0.47			0.85
<400	417 (67.48)	64 (71.91)		107 (69.48)	17 (73.91)	
≥400	201 (32.52)	25 (28.09)		47 (30.52)	6 (26.09)	

Table 1 (*continued*)

Table 1 (*continued*)

Feature	Development cohort			Test cohort		
	Non-PHT	PHT	P value	Non-PHT	PHT	P value
PIVKA-II (μg/L)	5,367.98±10,344.92	6,228.65±14,011.10	0.45	4,866.27±4,977.18	4,678.90±3,863.34	0.68
Liver fluke			0.21			0.09
Feminine character	473 (76.54)	64 (71.91)		120 (77.92)	16 (69.57)	
Weakly positive	62 (10.03)	7 (7.87)		8 (5.19)	4 (17.39)	
Positive	83 (13.43)	18 (20.22)		26 (16.88)	3 (13.04)	
SV (mm^3)	202,872.23±100,514.90	390,356.57±273,150.53	<0.001	227,370.38±123,624.37	434,484.70±253,936.50	<0.001
LV (mm^3)	1,316,280.30±373,654.21	1,309,202.94±398,792.82	0.71	1,347,538.18±397851.91	1,297,818.78±288,764.62	0.74
Liver tumor volume (mm^3)	187,329.72±288,238.23	191,042.74±327,058.81	0.07	194,386.91±339,030.83	63,119.55±112,830.65	0.002
Volume of liver non-tumor area (mm^3)	1,128,950.57±241,003.40	1,118,160.20±258,896.85	0.57	1,153,151.27±233,341.90	1,234,699.23±281,131.70	0.2
Volume proportion of liver tumors (%)	11.88±14.20	11.29±15.86	0.07	11.81±13.74	4.56±7.34	0.001
Volume proportion of liver non-tumor area (%)	88.12±14.20	88.71±15.86	0.07	88.19±13.74	95.44±7.34	0.001
PVD (mm)	14.17±2.02	16.66±2.13	<0.001	14.12±2.27	16.66±2.21	<0.001
SVD (mm)	10.12±1.45	11.87±1.83	<0.001	10.24±1.70	11.87±1.96	<0.001
Maximum tumor diameter (cm)	6.45±3.60	6.32±4.15	0.26	6.62±3.94	4.99±3.25	0.071
No. of liver segments invaded by tumors			0.97			0.3
1	257 (41.59)	39 (43.82)		67 (43.51)	16 (69.57)	
2	232 (37.54)	32 (35.96)		61 (39.61)	4 (17.39)	
3	64 (10.36)	9 (10.11)		13 (8.44)	2 (8.70)	
4	62 (10.03)	9 (10.11)		11 (7.14)	1 (4.35)	
5	3 (0.49)	0		1 (0.65)	0	
6	0	0		1 (0.65)	0	
CNLC			0.55			<0.001
Ia	254 (41.10)	43 (48.31)		58 (37.66)	18 (78.26)	
Ib	287 (46.44)	35 (39.33)		82 (53.25)	3 (13.04)	
IIa	56 (9.06)	6 (6.74)		11 (7.14)	0	
IIb	4 (0.65)	1 (1.12)		1 (0.65)	0	
IIIa	15 (2.43)	3 (3.37)		2 (1.30)	2 (8.70)	
IIIb	2 (0.32)	1 (1.12)		0	0	
BCLC			0.07			0.036
A	541 (87.54)	78 (86.52)		140 (90.91)	21 (91.30)	
B	60 (9.71)	8 (8.99)		12 (7.79)	0	
C	17 (2.75)	3 (3.37)		2 (1.30)	2 (8.70)	
Tumor number			0.59			0.32
Single	544 (88.03)	76 (85.39)		132 (85.71)	22 (95.65)	
Multiple	74 (11.97)	13 (14.61)		22 (14.29)	1 (4.35)	

Data are presented as n (%) or mean ± standard deviation. Non-PHT, non-portal hypertension; PHT, portal hypertension; AFP, alpha-fetoprotein; ALT, alanine aminotransferase; AST, aspartate aminotransferase; BCLC, Barcelona Clinic Liver Cancer Stage; BMI, body mass index; CNLC, China Liver Cancer Staging; LV, liver volume; PVD, portal vein diameter; SV, spleen volume; SVD, splenic vein diameter; NLR, neutrophil-to-lymphocyte ratio; Plt, platelet; Tbil, total bilirubin; Alb, albumin; INR, international normalized ratio; FIB-4, fibrosis 4 score; APRI, aspartate aminotransferase-to-platelet ratio index; PIVKA-II, protein induced by vitamin K absence or antagonist-II.

Table 2 Clinical features univariate and multifactorial logistic regression

Feature	Univariate			Multifactorial		
	OR	95% CI	P value	OR	95% CI	P value
Gender	0.948	0.894–1.006	0.14			
Age (years)	1.001	0.999–1.002	0.6			
BMI (kg/m^2)	1.004	0.998–1.011	0.27			
Diabetes	1.044	0.95–1.147	0.45			
NLR	1.014	0.998–1.03	0.15			
Plt (10^9/L)	0.999	0.999–0.999	0	1	1–1	0.56
Tbil (mmol/L)	1.007	1.005–1.008	0	1.002	1–1.004	0.1
Alb (g/L)	0.984	0.978–0.988	0	0.995	0.99–0.999	0.06
Ascites	1.073	1.018–1.13	0.026	0.954	0.906–1.005	0.13
AST (U/L)	1.001	1–1.001	0	1.001	1–1.001	0.27
ALT (U/L)	1.001	1–1.001	0.002	1	0.999–1	0.99
AST/ALT	1.004	0.992–1.016	0.61			
APRI	1.219	1.134–1.31	0	0.962	0.89–1.041	0.42
INR	1.647	1.362–1.992	0	1.081	0.909–1.285	0.46
Child Pugh	1.356	1.271–1.446	0	1.132	1.05–1.221	0.01
FIB-4 score	1.164	1.13–1.2	0	1.087	1.048–1.126	<0.001
Viral hepatitis B	1.004	0.959–1.05	0.89			
Viral hepatitis C	1.058	0.897–1.25	0.57			
Hepatitis B virus DNA	1	1–1	0.057			
AFP (ng/mL)	0.978	0.935–1.022	0.40			
PIVKA-II (μg/L)	1	1–1	0.49			
Liver fluke	1.024	0.996–1.054	0.16			
SV (mm^3)	1	1–1	<0.001	1	1–1	0
LV (mm^3)	1	1–1	0.87			
Liver tumor volume (mm^3)	1	1–1	0.91			
Volume of liver non-tumor area (mm^3)	1	1–1	0.7			
Volume proportion of liver tumors (%)	1	0.998–1.001	0.72			
Volume proportion of liver non-tumor area (%)	1	0.999–1.002	0.72			
PVD (mm)	1.059	1.049–1.068	0	1.027	1.015–1.04	<0.001
SVD (mm)	1.077	1.064–1.09	0	1.009	0.991–1.026	0.41
Maximum tumor diameter (cm)	0.999	0.993–1.005	0.75			
Number of liver segments invaded by tumors	0.996	0.975–1.017	0.73			
CNLC	0.996	0.973–1.02	0.8			
BCLC	1.016	0.969–1.065	0.58			

AFP, alpha-fetoprotein; ALT, alanine aminotransferase; AST, aspartate aminotransferase; BCLC, Barcelona Clinic Liver Cancer Stage; BMI, body mass index; CNLC, China Liver Cancer Staging; LV, liver volume; PVD, portal vein diameter; SV, spleen volume; SVD, splenic vein diameter; NLR, neutrophil-to-lymphocyte ratio; Plt, platelet; Tbil, total bilirubin; Alb, albumin; INR, international normalized ratio; FIB-4, fibrosis 4 score; APRI, aspartate aminotransferase-to-platelet ratio index; PIVKA-II, protein induced by vitamin K absence or antagonist-II.

Table 3 Performance evaluation of machine-learning algorithm models

Model feature	Accuracy	AUC (95% CI)	Sensitivity	Specificity	PPV	NPV	Precision	Recall	F1
Radiology feature									
LR									
Development cohorts	0.736	0.76 (0.701–0.819)	0.674	0.744	0.275	0.941	0.275	0.674	0.391
Test cohorts	0.701	0.834 (0.762–0.906)	0.826	0.682	0.279	0.963	0.279	0.826	0.418
KNN									
Development cohorts	0.887	0.903 (0.881–0.926)	0.596	0.929	0.546	0.941	0.546	0.596	0.57
Test cohorts	0.864	0.654 (0.532–0.777)	0.087	0.981	0.4	0.878	0.4	0.087	0.143
Random forest									
Development cohorts	0.832	0.815 (0.765–0.864)	0.629	0.861	0.394	0.942	0.394	0.629	0.485
Test cohorts	0.842	0.77 (0.676–0.864)	0.478	0.896	0.407	0.92	0.407	0.478	0.44
Pre-fusion feature									
LR									
Development cohorts	0.736	0.894 (0.858–0.931)	0.674	0.744	0.275	0.941	0.275	0.674	0.391
Test cohorts	0.701	0.768 (0.667–0.869)	0.826	0.682	0.279	0.963	0.279	0.826	0.418
KNN									
Development cohorts	0.887	0.911 (0.889–0.933)	0.596	0.929	0.546	0.941	0.546	0.596	0.57
Test cohorts	0.864	0.634 (0.515–0.753)	0.087	0.981	0.4	0.878	0.4	0.087	0.143
Random forest									
Development cohorts	0.832	0.855 (0.809–0.901)	0.629	0.861	0.394	0.942	0.394	0.629	0.485
Test cohorts	0.842	0.666 (0.536–0.796)	0.478	0.896	0.407	0.92	0.407	0.478	0.44
Clinical features									
LR									
Development cohorts	0.829	0.859 (0.819–0.899)	0.854	0.825	0.413	0.975	0.413	0.854	0.557
Test cohorts	0.672	0.854 (0.779–0.929)	0.739	0.662	0.246	0.944	0.246	0.739	0.37
KNN									
Development cohorts	0.895	0.933 (0.915–0.951)	0.596	0.939	0.582	0.942	0.582	0.596	0.589
Test cohorts	0.825	0.733 (0.617–0.85)	0.261	0.909	0.3	0.892	0.3	0.261	0.279
Random forest									
Development cohorts	0.823	0.875 (0.837–0.913)	0.742	0.835	0.393	0.957	0.393	0.742	0.514
Test cohorts	0.672	0.84 (0.758–0.921)	0.609	0.682	0.222	0.921	0.222	0.609	0.326

LR, logistic regression; KNN, K-nearest neighbor; AUC, area under the curve; CI, confidence interval; PPV, positive predictive value; NPV, negative predictive value.

conducted an in-depth exploration of CT images of non-tumorous liver areas during the portal venous phase, employing radiomics and deep-learning techniques for feature extraction and selection. Baseline data with partial differences between the PHT and non-PHT groups, considering that these data may have an impact on treatment decisions. Therefore, we compared the diverging baseline data with imaging features combined with individual or joint modeling to build the best predictive model. Based on these extensive data, we successfully developed the following

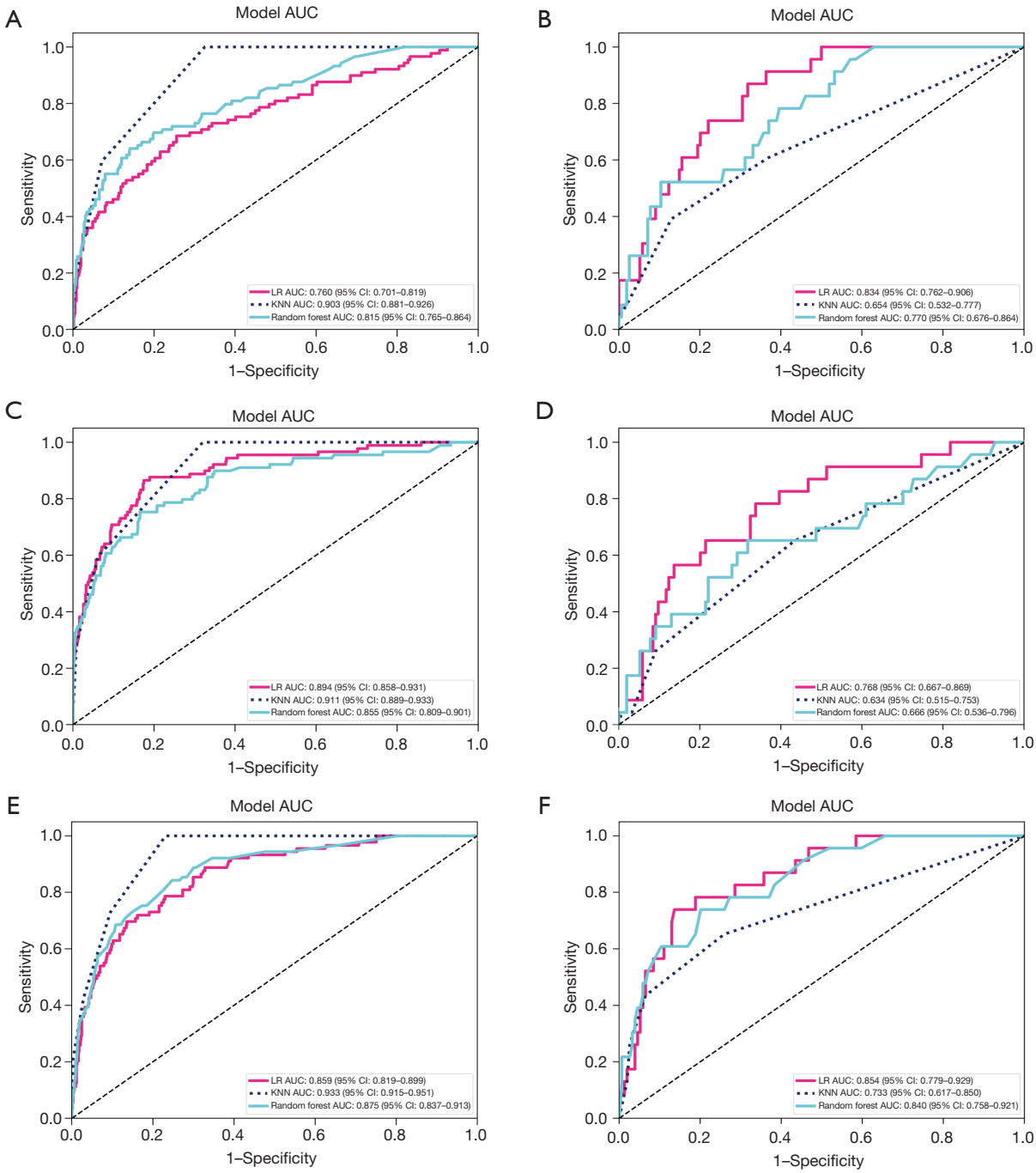

Figure 2 Performance evaluation of the machine-learning algorithm models. (A,B) Radiology feature: (A) Development cohorts, (B) test cohorts; (C,D) pre-fusion feature: (C) development cohorts, (D) test cohorts; (E,F) clinical features: (E) development cohorts; (F) test cohorts. AUC, area under the curve; LR, logistic regression; KNN, K-nearest neighbor; CI, confidence interval.

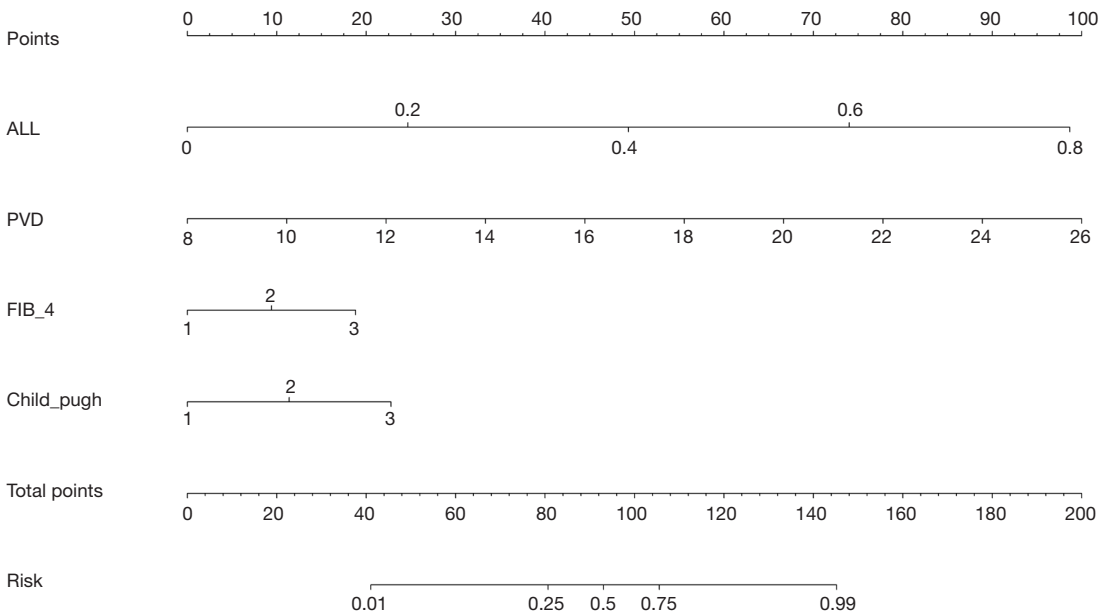

Figure 3 Pre-feature fusion linear model based on radiology features, deep-learning features and clinical features. PVD, portal vein diameter; FIB-4, fibrosis 4 score; ALL, prediction probability after fusion of deep learning and image omics features; Child_pugh 1/2/3, Child_pugh A/B/C.

Table 4 Comparison of model prediction efficiency

Model	Accuracy	AUC (95% CI)	Sensitivity	Specificity	PPV	NPV	Precision	Recall	F1
Development cohorts									
Clinic	0.883	0.933 (0.915–0.951)	0.73	0.905	0.524	0.959	0.524	0.73	0.61
Rad	0.887	0.903 (0.881–0.926)	0.596	0.929	0.546	0.941	0.546	0.596	0.57
DTL	0.781	0.832 (0.788–0.876)	0.73	0.788	0.332	0.953	0.332	0.73	0.456
Combined	0.895	0.911 (0.889–0.933)	0.596	0.939	0.582	0.942	0.582	0.596	0.589
Nomogram	0.861	0.966 (0.954–0.979)	0.966	0.846	0.475	0.994	0.475	0.966	0.637
Test cohorts									
Clinic	0.87	0.733 (0.617–0.85)	0.435	0.935	0.5	0.917	0.5	0.435	0.465
Rad	0.864	0.654 (0.532–0.777)	0.087	0.981	0.4	0.878	0.4	0.087	0.143
DTL	0.661	0.623 (0.504–0.743)	0.565	0.675	0.206	0.912	0.206	0.565	0.302
Combined	0.825	0.634 (0.515–0.753)	0.261	0.909	0.3	0.892	0.3	0.261	0.279
Nomogram	0.729	0.698 (0.565–0.831)	0.609	0.747	0.264	0.927	0.264	0.609	0.368

Clinic, clinical features; Rad, radiology features; DTL, deep (transfer) learning; Combined, radiology features and deep-learning features pre-fusion; AUC, area under the curve; CI, confidence interval; PPV, positive predictive value; NPV, negative predictive value.

five predictive models: a clinical feature-based predictive model; a radiomics feature-based predictive model; a pre-fusion feature-based predictive model; a nomogram that integrates radiomics features, deep-learning features, and clinical features through pre-fusion in a linear manner; and a deep learning-based model. Among these models, the nomogram exhibited particularly outstanding performance in the training set (AUC: 0.966), demonstrating excellent

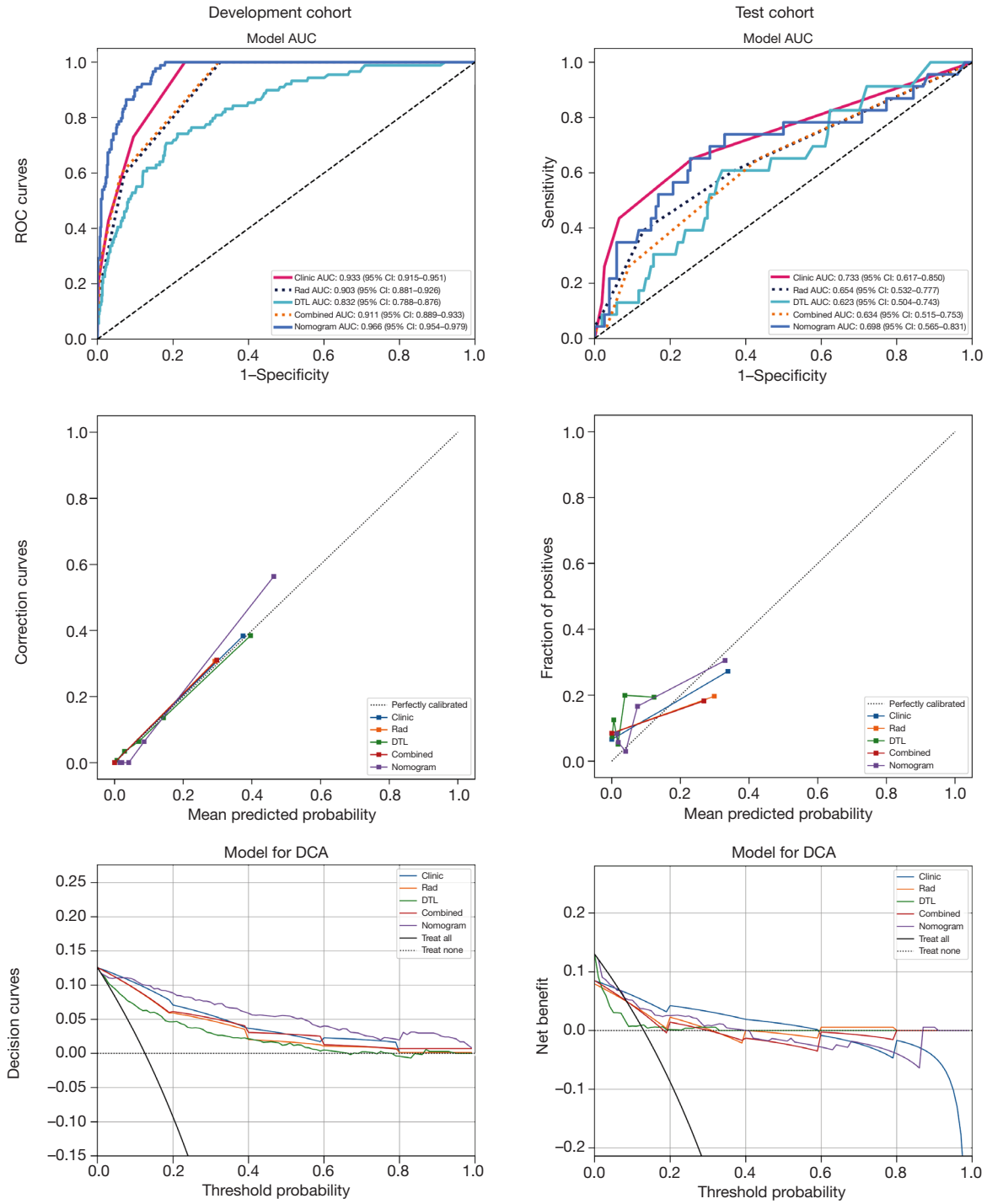

Figure 4 Performance evaluation of machine-learning algorithm models. From top to bottom are ROC curve, correction curve and clinical decision curve respectively. Clinic, clinical features; Rad, radiology features; DTL, deep (transfer) learning; Combined, radiology features and deep-learning features pre-fusion; ROC, receiver operating characteristic; AUC, area under the curve; CI, confidence interval; DCA, decision curve analysis.

predictive capability. The AUC of the Nomogram decreased significantly from the training set (AUC: 0.966) to the test set (AUC: 0.698), indicating potential overfitting problems. This may be because the training set data is too complex or noisy, and the model does not generalize effectively to the test set. In addition, improper feature selection, excessive model complexity, or large differences in the distribution of test sets and training sets may also lead to this phenomenon. Overall, the predictive performance of each feature model in the training group was higher than that in the validation group.

Recent research has shown that radiomics has significant potential as a means of comprehensively analyzing organ changes through imaging examinations. Zhao *et al.* used CT-based imaging scores to predict re-bleeding and mortality in HCC patients with PHT after acute variceal bleeding (23). Similarly, Yu *et al.* developed a non-invasive prediction tool based on spleen volume to aid in predicting liver decompensation in patients with compensated cirrhosis without the need for HVPG measurements (24). Further, Liu *et al.* designed a model incorporating texture features, morphological features, and volumes of both the liver and spleen, which significantly outperformed models using the liver stiffness measurement and other radiological and clinical indicators when HVPG was used as the reference standard (25). These studies showed the effectiveness of CT-based radiomics analysis in predicting PHT. However, there is still a significant gap in research on PHT patients with HCC. This study adopted a unique approach by conducting an in-depth analysis of non-tumorous liver areas and successfully constructed a predictive model with excellent performance.

Deep learning is a branch of machine learning with extensive applications in various fields of image analysis (26). In the medical profession, deep learning is most widely applied in radiology and pathology, and it can be used to extract data from medical images that are not readily apparent to human analysts, which can inform results related to molecular status, prognosis, or treatment sensitivity (27). One of the main advantages of 2.5-dimensional (2.5D) imaging in deep learning is its ability to incorporate spatial context from adjacent slices, which can improve detection and segmentation accuracy compared to traditional 2D models. A study developed a 2.5D deep-learning object detection model for the automatic detection of brain metastases, which demonstrated better performance than 2D models by reducing false positives and increasing the positive predictive value (28). Additionally, 2.5D methods can address issues related to building deep-learning models on small datasets. Another study combined transfer learning strategies with 2.5D data slicing strategies, and successfully improved the ability of the model to segment contrast-enhanced lesions in brain magnetic resonance imaging scans, demonstrating the effectiveness of 2.5D imaging in situations with limited data (29). Given the advantages of deep learning, our study adopted algorithms based on 2.5D deep learning, and the multiple predictive models constructed exhibited good predictive performance. The poor performance of the 2.5D deep learning test set can be attributed to the differences in data distribution and weak generalization due to insufficient training; The complexity of the model is too high, and the parameters are inappropriate, resulting in overfitting. Improper feature selection and high dimension affect performance; lack of biological significance feature extraction; the test set is improperly set or the model is overfitted. It is necessary to optimize the data, adjust the model, improve the feature extraction, combine the advantages of radionics, and rationally set the test set to improve the performance.

Further, our study also explored the independent and combined application effects of radiomics features and deep-learning features in predictive models. We found that the pre-fusion model that combined radiomics features and deep-learning features exhibited superior predictive performance on the training set compared to either feature set alone. Its performance on the test set was slightly inferior to that of the radiomics model; however, it still outperformed the deep-learning model.

The exceptional performance of the fusion model on the training set may be attributed to the complementarity between radiomics features and deep-learning features. Radiomics features typically rely on the statistical and texture analysis of images to capture macroscopic structural information, while deep-learning features learn more abstract and deeper representations of images through neural networks (30-32). The combination of these two types of features may provide richer information for prediction tasks, thus achieving higher accuracy on training sets. Our study used a method that combined clinical features with radiomics features and deep-learning (2.5D) features to predict the occurrence of PHT from multiple dimensions, which is also one of the innovative points of this study.

Surgical resection is currently the preferred treatment for patients with HCC, but clinically significant PHT increases the risk of postoperative liver failure, and was once

considered a contraindication for liver resection. However, with advancements in surgical techniques and perioperative management, postoperative complications have been significantly reduced. Existing HCC guidelines recommend extending liver resection to HCC patients with clinically significant PHT. However, accurately selecting the optimal candidates for liver resection remains a challenge that needs to be addressed urgently. Liver transplantation can simultaneously address both the tumor and PHT issues, but the shortage of liver donors and high costs make its practical application difficult (33,34). Another option is to administer systemic drug therapy and/or combined hepatic artery infusion chemotherapy, but the disease control rate is limited (35). Our predictive model can identify HCC patients with PHT early, allowing for the formulation of personalized treatment strategies to optimize their treatment outcomes and improve prognosis. Imaging and deep learning predictive models face many challenges in clinical practice, including the high cost of data acquisition and annotation, poor model interpretability, difficult integration of clinical workflow, resource constraints, and large professional training needs. These challenges limit the clinical translation and wide application of the model and require interdisciplinary collaboration and ongoing research to overcome.

Our study made some new discoveries, but it also had some limitations. First, due to the relatively small number of PHT cases, the model performance on the test set was not ideal, especially in the training of the deep-learning models, where its powerful learning and generalization capabilities could not be fully utilized. To some extent, this limited our comprehensive evaluation and optimization of model performance. The image quality of imaging is affected by equipment, procedure, and patient conditions, which may lead to inaccurate diagnosis. In addition, the interpretation of imaging features is subjective and may vary between different observers. Predictive models are limited by data quality, sample selection bias, and model generalization ability. Incomplete data or noise can degrade model performance while overfitting can cause the model to perform poorly on new data. Therefore, these factors should be considered comprehensively to improve the accuracy and reliability of imaging diagnosis and prediction models. Visual representations such as feature importance heat maps and confusion matrices can visually show the feature contributions and classification performance of models, significantly improving the interpretability of deep learning models. However, the goal of our research is to build efficient predictive models.

Conclusions

In summary, we found that among our various predictive models, our nomogram model that combined clinical features with radiomics features of non-tumor liver areas and deep-learning features outperformed the radiomics models, deep-learning models, and combined radiomics deep-learning models. Compared to the clinical prediction models, our model showed improved predictive performance on the training set. Our predictive model is easy to apply and provides a basis for clinical decision making in HCC patients with PHT. Further research needs to be conducted to explore the universal utility of our model and apply it in clinical practice.

Acknowledgments

None.

Footnote

Reporting Checklist: The authors have completed the TRIPOD reporting checklist. Available at https://jgo.amegroups.com/article/view/10.21037/jgo-2024-931/rc

Data Sharing Statement: Available at https://jgo.amegroups.com/article/view/10.21037/jgo-2024-931/dss

Peer Review File: Available at https://jgo.amegroups.com/article/view/10.21037/jgo-2024-931/prf

Funding: This study was supported by the China Postdoctoral Science Foundation (No. 2023M744020), the Shenzhen Municipal Science and Technology Innovation Committee (No. JCYJ20220818103407016), the Shenzhen Basic Research Funding Project (Nos. JCYJ20220530144404010 and JCYJ20220530144404011), the Futian District Health System Research Project (No. FTWS2023037), the Medical Excellence Award Funded by the Creative Research Development Grant from the First Affiliated Hospital of Guangxi Medical University (No. 2021006), the First-Class Discipline Innovation-Driven Talent Program of Guangxi Medical University, Guangxi Medical and Health Appropriate Technology Development and Application Project (Nos. S2021100 and S2022065), the National Natural Science Foundation

of China (Nos. 81802874 and 82260548), the Natural Science Foundation of the Guangxi Province of China (No. 2024GXNSFAA010347), the Guangxi Key R&D Program (No. GKEAB18221019).

Conflicts of Interest: All authors have completed the ICMJE uniform disclosure form (available at https://jgo.amegroups.com/article/view/10.21037/jgo-2024-931/coif). The authors have no conflicts of interest to declare.

Ethical Statement: The authors are accountable for all aspects of the work in ensuring that questions related to the accuracy or integrity of any part of the work are appropriately investigated and resolved. The study was reviewed and approved by the Ethics Committee of the First Affiliated Hospital of Guangxi Medical University (No. 2023-E488-01). The study was conducted in accordance with the Declaration of Helsinki (as revised in 2013). Because the patient data were collected retrospectively, informed consent was not required.

References

1. Singal AG, Kanwal F, Llovet JM. Global trends in hepatocellular carcinoma epidemiology: implications for screening, prevention and therapy. Nat Rev Clin Oncol 2023;20:864-84.
2. Shelat VG. Poor prognosis of hepatocellular carcinoma patients-how, why, and what? J Gastrointest Oncol 2024;15:2372-5.
3. Guidelines for diagnosis and treatment of primary liver cancer in China (2019 edition). Zhonghua Gan Zang Bing Za Zhi 2020;28:112-28.
4. Allaire M, Rudler M, Thabut D. Portal hypertension and hepatocellular carcinoma: Des liaisons dangereuses…. Liver Int 2021;41:1734-43.
5. Thabut D, Kudo M. Treatment of portal hypertension in patients with HCC in the era of Baveno VII. J Hepatol 2023;78:658-62.
6. Allaire M, Thabut D. Portal hypertension and variceal bleeding in patients with liver cancer: Evidence gaps for prevention and management. Hepatology 2024;79:213-23.
7. De Gaetano V, Pallozzi M, Cerrito L, et al. Management of Portal Hypertension in Patients with Hepatocellular Carcinoma on Systemic Treatment: Current Evidence and Future Perspectives. Cancers (Basel) 2024;16:1388.
8. Xu XF, Xing H, Han J, et al. Risk Factors, Patterns, and Outcomes of Late Recurrence After Liver Resection for Hepatocellular Carcinoma: A Multicenter Study From China. JAMA Surg 2019;154:209-17.
9. Takemura N, Kokudo N. Relationship between portal hypertension and liver stiffness measurements in the treatment of hepatocellular carcinoma from the surgeon's point of view in the Baveno VII era. Hepatobiliary Surg Nutr 2024;13:150-3.
10. Bosch J, Abraldes JG, Berzigotti A, et al. The clinical use of HVPG measurements in chronic liver disease. Nat Rev Gastroenterol Hepatol 2009;6:573-82.
11. Bi WL, Hosny A, Schabath MB, et al. Artificial intelligence in cancer imaging: Clinical challenges and applications. CA Cancer J Clin 2019;69:127-57.
12. Li M, Fan Y, You H, et al. Dual-Energy CT Deep Learning Radiomics to Predict Macrotrabecular-Massive Hepatocellular Carcinoma. Radiology 2023;308:e230255.
13. Ji K, Zhu H, Zhang C, et al. Nomogram-based prognostic stratification for patients with large hepatocellular carcinoma: a population study of SEER database and a Chinese cohort. J Gastrointest Oncol 2024;15:2201-15.
14. Li L, Liu C, Li H, et al. Development and validation of a nomogram to predict cancer-specific survival of patients with large hepatocellular carcinoma accepting surgical resection: a real-world analysis based on the SEER database. J Gastrointest Oncol 2024;15:1657-73.
15. Huang YQ, Liang CH, He L, et al. Development and Validation of a Radiomics Nomogram for Preoperative Prediction of Lymph Node Metastasis in Colorectal Cancer. J Clin Oncol 2016;34:2157-64.
16. Huang Y, Liu Z, He L, et al. Radiomics Signature: A Potential Biomarker for the Prediction of Disease-Free Survival in Early-Stage (I or II) Non-Small Cell Lung Cancer. Radiology 2016;281:947-57.
17. Liu Z, Zhang XY, Shi YJ, et al. Radiomics Analysis for Evaluation of Pathological Complete Response to Neoadjuvant Chemoradiotherapy in Locally Advanced Rectal Cancer. Clin Cancer Res 2017;23:7253-62.
18. Zhang B, Tian J, Dong D, et al. Radiomics Features of

Multiparametric MRI as Novel Prognostic Factors in Advanced Nasopharyngeal Carcinoma. Clin Cancer Res 2017;23:4259-69.
19. Foersch S, Glasner C, Woerl AC, et al. Multistain deep learning for prediction of prognosis and therapy response in colorectal cancer. Nat Med 2023;29:430-9.
20. Calderaro J, Seraphin TP, Luedde T, et al. Artificial intelligence for the prevention and clinical management of hepatocellular carcinoma. J Hepatol 2022;76:1348-61.
21. Zeng Q, Klein C, Caruso S, et al. Artificial intelligence-based pathology as a biomarker of sensitivity to atezolizumab-bevacizumab in patients with hepatocellular carcinoma: a multicentre retrospective study. Lancet Oncol 2023;24:1411-22.
22. Han W, Qin L, Bay C, et al. Deep Transfer Learning and Radiomics Feature Prediction of Survival of Patients with High-Grade Gliomas. AJNR Am J Neuroradiol 2020;41:40-8.
23. Zhao M, Zhang B, Shi J, et al. HCC portal hypertension imaging score derived from CT predicts re-bleeding and mortality after acute variceal bleeding. Cancer Imaging 2024;24:45.
24. Yu Q, Xu C, Li Q, et al. Spleen volume-based non-invasive tool for predicting hepatic decompensation in people with compensated cirrhosis (CHESS1701). JHEP Rep 2022;4:100575.
25. Liu Y, Ning Z, Örmeci N, et al. Deep Convolutional Neural Network-Aided Detection of Portal Hypertension in Patients With Cirrhosis. Clin Gastroenterol Hepatol 2020;18:2998-3007.e5.
26. Anwar SM, Majid M, Qayyum A, et al. Medical Image Analysis using Convolutional Neural Networks: A Review. J Med Syst 2018;42:226.
27. Levine AB, Schlosser C, Grewal J, et al. Rise of the Machines: Advances in Deep Learning for Cancer Diagnosis. Trends Cancer 2019;5:157-69.
28. Takao H, Amemiya S, Kato S, et al. Deep-learning 2.5-dimensional single-shot detector improves the performance of automated detection of brain metastases on contrast-enhanced CT. Neuroradiology 2022;64:1511-8.
29. Huang L, Zhao Z, An L, et al. 2.5D transfer deep learning model for segmentation of contrast-enhancing lesions on brain magnetic resonance imaging of multiple sclerosis and neuromyelitis optica spectrum disorder. Quant Imaging Med Surg 2024;14:273-90.
30. LeCun Y, Bengio Y, Hinton G. Deep learning. Nature 2015;521:436-44.
31. Gillies RJ, Kinahan PE, Hricak H. Radiomics: Images Are More than Pictures, They Are Data. Radiology 2016;278:563-77.
32. Litjens G, Kooi T, Bejnordi BE, et al. A survey on deep learning in medical image analysis. Med Image Anal 2017;42:60-88.
33. Bhangui P, Allard MA, Vibert E, et al. Salvage Versus Primary Liver Transplantation for Early Hepatocellular Carcinoma: Do Both Strategies Yield Similar Outcomes? Ann Surg 2016;264:155-63.
34. de Haas RJ, Lim C, Bhangui P, et al. Curative salvage liver transplantation in patients with cirrhosis and hepatocellular carcinoma: An intention-to-treat analysis. Hepatology 2018;67:204-15.
35. Balducci D, Montori M, De Blasio F, et al. The Role of Transjugular Intrahepatic Portosystemic Shunt (TIPS) in Treating Portal Hypertension in Patients with Hepatocellular Carcinoma. Medicina (Kaunas) 2023;59:1150.

Cite this article as: He Y, Gao Q, Mo S, Huang K, Liao Y, Liang T, Chen M, Wang J, Tao Q, Zhang G, Wu F, Han C, Shi X, Peng T. Artificial intelligence algorithm was used to establish and verify the prediction model of portal hypertension in hepatocellular carcinoma based on clinical parameters and imaging features. J Gastrointest Oncol 2025;16(1):159-175. doi: 10.21037/jgo-2024-931